RSC Advances

ROYAL SOCIETY OF CHEMISTRY

www.rsc.org/advances

Titanium Incorporated with UiO-66(Zr)-type Metal-Organic Framework (MOF) for Photocatalytic Application

Aoning Wang,[1] Yingjie Zhou,[2] Zhoulu Wang,[1] Miao Chen,[1] Luyi Sun,[3] Xiang Liu[1*]

[1] Key Laboratory of Flexible Electronics (KLOFE) & Institute of Advanced Materials (IAM), National Jiangsu Synergistic Innovation Center for Advanced Materials (SICAM), Nanjing Tech University (Nanjing Tech), 30 South Puzhu Road, Nanjing, Jiangsu 211816, China

[2] School of Physics and Optoelectronic Engineering, Nanjing University of Information Science & Technology, 219 Ningliu Road, Nanjing, Jiangsu 210044, China

[3] Department of Chemical & Biomolecular Engineering and Polymer Program, Institute of Materials Science, University of Connecticut, Storrs, Connecticut 06269, United States

*Authors to whom correspondence should be addressed:

Dr. Xiang Liu, Email: iamxliu@njtech.edu.cn

Abstract:

A UiO-66-type metal-organic framework (MOF) fabricated by titanium was successfully prepared via a facial modified post-grafting method. The as-prepared samples were characterized by X-ray photoelectron spectroscopy (XPS), X-ray diffraction (XRD), transmission electron microscopy (TEM), scanning electron microscopy (SEM), ultraviolet-visible adsorption spectroscopy (UV-vis), and photoluminescence spectroscopy (PL) techniques. The introduction of titanium enhanced the optical properties of UiO-66 via the formation of oxo-bridged hetero-Zr-Ti clusters, but leading to a sacrifice in crystallinity. The removal of methylene blue (MB) over these samples could be attributed to the dual function of the adsorption and photo-degradation mechanisms. The highest MB removal efficiency of 87.1% was achieved over UiO-66(1.25Ti) under simulated sun-light irradiation.

Keywords: photocatalysis, MOFs, titanium, UiO-66

1. Introduction

Metal-organic frameworks (MOFs), constructed from the assembly of metallic ions and organic ligands, are a new class of highly crystalline and porous material with an extended 3D network. MOFs have attracted tremendous interest due to their intriguing aesthetic structures and outstanding properties, such as high surface area, tunable crystalline structure and pore size, and functionality.[1] Up to date, MOFs have been employed in a wide range of promising applications, such as catalysis,[2, 3] gas storage/separation/adsorption,[4-10] drug delivery,[11, 12] pollutants removal,[13-16] sensors,[16-18] and so on. Among these applications, catalysis has been particularly interesting and attracted increasing attention.

Nowadays, photocatalysis has been the subject of a huge amount of studies related to air cleaning and water purification, because it offers a great potential for completely decomposing toxic chemicals,[19] and thus fulfill our expectations to create a clean future in utilizing solar energy. MOFs have already been used for new heterogeneous photocatalytic materials owing to their ligand-to-metal charge transfer states,[20, 21] and they exhibit superior performance to traditional photocatalyst systems.[1, 16, 22-25] Especially, the band gap in MOFs is closely related to the HOMO–LUMO gap and the energy transfer can take place from the organic linker to the metal-oxo cluster within some MOFs under light illumination.[22] The incorporation with photoactive species in MOFs is considered one of the effective ways to use the solar light, besides the modification of the metal ions or the organic ligands.[26] The high photocatalytic activities not only lie in the

highly porous crystalline nature of the MOFs, but also because the narrow micro-pore distribution of MOFs may lead to the monodispersed photoactive species anchored on MOFs.[21] Additionally, the MOFs can provide extra pathways for the migration of photo-induced electrons, and thus facilitate the charge carrier separation.[1, 22, 25]

In recent years, much dye-containing wastewater was produced in textile, paper, and printing industries. Dyes are generally very stable to light and oxidation due to the complex aromatic molecular structures, but this causes damage to the environment and dramatically threatens human health.[27-29] Therefore, the effective treatment of these wastewater is one of the most crucial problems before releasing them into the environment. Hitherto, various techniques have been explored to remove the dyes from wastewater, including adsorption,[30] photo-degradation,[31] flocculation,[32] electrolysis,[33] and biodegradation.[34] Adsorption and photo-degradation are considered the most competitive techniques among all of these applications, because they have the advantages of low cost, high efficiency, and environment-friendly. The reported adsorbents,[30, 35, 36] such as zeolite, activated carbon, have in common the big surface area and physical and chemical stability. On the other hand, numerous semiconductors have been employed as photocatalysts for the dye removal.[37-39] However, the dye removal efficiency by adsorbents relies on their capacity and specific surface areas. The photodegradation efficiency mainly depends on the photocatalytic activities of photocatalysts, which is usually hindered by the agglomeration of the ultrafine powders [40]. The combination of photodegradation with adsorption method should be one of the most promising ways to

enhance the dye removal efficiency, i.e., cooperating the photocatalysts on adsorbents without sacrificing their porous properties.

Recently, MOFs have been investigated as selective dye adsorbents because of their high specific surface area and uniform but tunable pore size.[13, 15, 41, 42] In addition, noble metals and some semiconductors have been incorporated into MOFs for certain photocatalytic reactions, such as dual modification of CdS and MoS_2 with UiO-66 for photocatalytic H_2 production,[1] Pd@UiO-66(NH_2) nanocomposite on the reduction of Cr(VI) to Cr(III) under mild conditions, etc..[22] UiO-66 is a zirconium containing MOF, and it behaves as an excellent photoactive species carrier due to its highly stable, adjustable and photoactive properties. Toward this end, we herein report the synthesis of titanium cooperated with UiO-66 (UiO-66(Ti)) via a facial modified post-grafting method. The photocatalytic performance of the as-synthesized UiO-66(Ti) nanocomposites was evaluated using the removal of methylene blue (MB) under the simulated sun-light irradiation.

2. Experimental

2.1 Materials

Zirconyl chloride octahydrate ($ZrOCl_2 \cdot 8H_2O$, 98%), 1,4-benzenedicarboxylic acid (PTA), isopropanol, triethylamine, and tetrabutyl titanate ($Ti(OBu)_4$) were ordered from Aladdin and used as received. Reagent-grade methanol, *N,N*-dimethylformamide (DMF), hydrochloric acid (HCl, 37 wt%), and toluene were obtained from common commercial

sources and used as received.

2.2 Synthesis of UiO-66

Sample UiO-66 was synthesized via the procedures reported in the literatures.[22, 41, 43] In a typical synthesis, 0.326 g of $ZrOCl_2 \cdot 8H_2O$ and 0.169 g of 1,4-benzenedicarboxylic acid were dissolved in 50 mL DMF with the assistance of ultrasonication. Subsequently, 0.5 mL HCl was added drop-wisely to the above obtained solution, which was then sealed in a 100 mL Teflon-lined pressure vessel for 24 h at 120 °C. After cooling to room temperature, the resulting solid was purified with methanol for several times, followed by drying under vacuum for 24 h at 100 °C.

2.3 Fabrication of UiO-66 with Titanium (Ti) (UiO-66(Ti))

The UiO-66(Ti) nanocomposites were synthesized via a modified post-grafting method according to the following procedures.[43, 44] Firstly, appropriate amount of $Ti(OBu)_4$ was mixed with the as-prepared UiO-66 in toluene, and then the mixture was heated at 100 °C for 24 h under N_2 flow. After that, the obtained sample was washed with toluene for several times and dried in air. UiO-66(Ti) samples with various Ti/Zr molar ratios were prepared, and they were denoted as UiO-66(nTi) (n=0.25:1, 0.5:1, 0.75:1, 1:1, 1.25:1, and 1.5:1), respectively.

2.4 Characterization

X-ray photoelectron spectroscopy (XPS) spectra were recorded on a PHI 5000 VersaProbe photoelectron spectrometer with monochromatic Al Kα radiation operated at 150 W. The shift of the binding energy due to the surface electrostatic charging was corrected using the C*1s* as an internal standard at 284.6 eV.

X-ray diffraction (XRD) was performed on a Rigaku Smartlab TM 9KW diffractometer between 5 to 50° with Cu Kα (λ=0.154059 nm) at 40 kV and 100 mA.

The specific surface area was obtained using a Micromeritics 3Flex. The samples were heated at 150 °C for 4 h prior to each test.

The morphological properties of the prepared samples were imaged by scanning

electron microscope (SEM, JSM-6360LV) operated at 15 kV.

The transmission electron microscopy (TEM) was observed on a HT7700 microscope with an accelerating voltage of 200 kV. The particles were dispersed in the mixture of ethanol and water, followed by being deposited on a carbon-film supported copper grid and air dried prior the measurement.

The Brunauer–Emmett–Teller surface areas (S_{BET}) were collected by N_2 adsorption isotherm using a Micromeritics 3Flex analyzer (Micromeritics Instrument Corporation, Norcross, GA, USA) at 77 K.

Ultraviolet-visible (UV-vis) absorbance spectra were collected on a Lambda 950 UV-vis-NIR spectrophotometer over a range of 250-700 nm.

The photoluminescence (PL) spectra were recorded on a Hitachi F-4600 FL fluorescence spectrophotometer at room temperature using Hg-Cd laser as an excitation light source. The excitation wavelength is 300 nm.

2.5 Photocatalytic measurement

The removal of a model pollutant methylene blue (MB) was investigated over the UiO-66(Ti) nanocomposites under a 250 W Xe lamp. In a typical process, a sample (50 mg) was first well dispersed in 50 mL MB solution (10 mg/L), followed by the exposure to the simulated sun light under continues stirring. Once the light illumination began, 3.5 mL of each sample was collected from the suspension solution at an interval of 10 min. After the catalyst was separated by a syringe filter (0.45 μm), the relative concentration of the supernatant solution was determined by the UV-vis absorbance at 572 nm.

3. Results and discussion

Figure 1 presents the XRD patterns of the UiO-66 and UiO-66(Ti) nanocomposite. UiO-66 exhibited a similar XRD pattern as reported in the literature.[45, 46] All the

UiO-66(Ti) nanocomposites possess similar XRD patterns as UiO-66, which indicates that the framework of UiO-66 is not altered with the introduction of titanium. However, no diffraction peaks belonged to titanium species could be observed even at a higher Ti concentration. Meanwhile, the diffraction peak at 2θ at around 7.3° shifts to a lower value as the Ti/Zr increases. These features imply that the titanium species are not simply grafted or encaged in the UiO-66 framework. Instead, the titanium species might be cooperated with Zr to the formation of oxo-bridged hetero-Zr-Ti clusters, which act as the skeleton of the UiO-66(Ti) framework.[43, 45-47] Particularly, when the molar ratio of Zr to Ti is 1/1, most of the characteristic peaks assigned to UiO-66 disappeared, indicating the loss of its well-ordered porous structure. Such phenomena suggest the shrinking of the crystal lattice because of the partial substitution of larger Zr in Zr-O oxo-clusters by smaller Ti[43]. The imbalance atom size of the Zr and Ti would not result in the uniform porous structures. However, the characteristics peaks of UiO-66 reappear when the molar ratio of Ti/Zr is 1.5/1. This suggests that most of the Zr would be substituted by the titanium species, which lead to the reformation of the UiO-66 framework with Ti-O clusters as the skeleton.

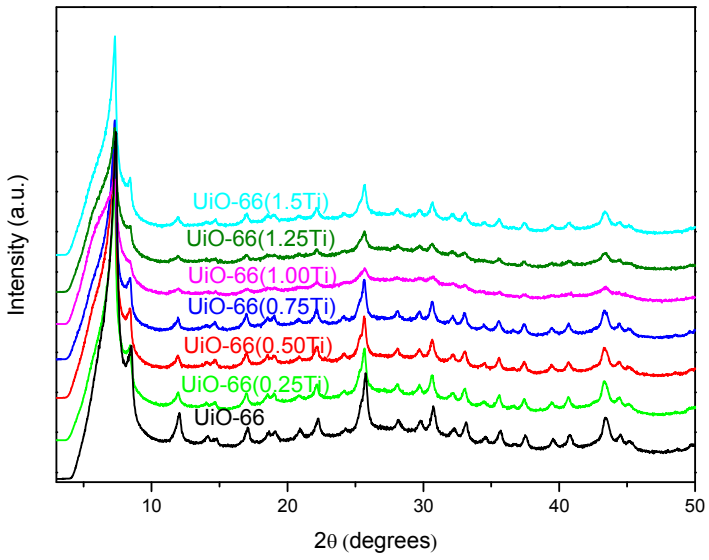

Figure 1. XRD patterns of UiO-66 and UiO-66(Ti) with various Ti/Zr molar ratios.

The X-ray photoelectron spectroscopy (XPS) is a highly sensitive technique to explore the chemical changes in the element surroundings. The XPS spectra of the elements of interest, i.e., Zr *3d*, Ti *2p*, and O *1s*, are shown in Figure 2. Figure 2(a) presents the survey scan of the UiO-66 and UiO-66(Ti) nanocomposites. As shown in Figure 2(a), new peaks associated with Ti *2p* appeared in the XPS spectrum of the UiO-66(Ti) nanocomposites, and their relative peak intensities to that of Zr *3p* increased with an increasing Ti content. These observations confirmed that the titanium moieties were successfully incorporated into UiO-66. In addition, the surface Ti/Zr molar ratios obtained by the XPS technique are presented in Table 1. It seems that the surface Ti/Zr molar ratios is higher than that of the bulk UiO-66(nTi). To be noted, the XPS is a highly surface sensitive instrument, the surface Ti/Zr molar ratios presented here is different from that of the bulk materials. These information also indicate that the $Ti(OBu)_4$ was easy to incorporate with the surface of the UiO-66. According to the high resolution scan spectra of Zr, Ti, and O atoms presented in Figure 2(b)-(d), the binding energies of Zr *3d,* Ti *2p*, and O *1s* shift to lower values as the concentration of Ti increases in the nanocomposites, suggesting the changes in the chemical environments of these elements. Binding energy depends on shielding effect caused by the electron density around atoms. Hence, the drop in the binding energy of Zr *3d* and Ti *2p* could be attributed to the enhanced electron density around Zr and Ti atoms, which might result from the weaker electronegativity of the strong interaction between Zr and Ti. Moreover, the binding energy of O *1s* in UiO-66(Ti) could be deconvoluted into three peaks centered at 530.9, 530.1, and 529.3 eV by Gaussian fitting, which corresponds to the contributions from the surface adsorbed hydroxyl groups, Zr-O,[47, 48] and Ti-O,[49, 50] respectively. The decreased binding energy of O *1s* with increasing Ti contents could also be explained by the enhanced electron density around the O atoms. All these features imply that the titanium

moieties be introduced to the framework of UiO-66 as electron donor via the formation of oxo-bridged hetero-Zr-Ti clusters.[43, 45-47]

Table 1. Surface molar ratios of Ti/Zr in UiO-66(nTi).

Samples	Ti (At%)	Zr (At%)	Surface Ti/Zr molar ratios
UiO-66	0	6.35	0
UiO-66(0.25Ti)	2.40	5.09	0.47
UiO-66(1Ti)	5.94	4.67	1.27
UiO-66(1.25Ti)	5.79	4.36	1.32

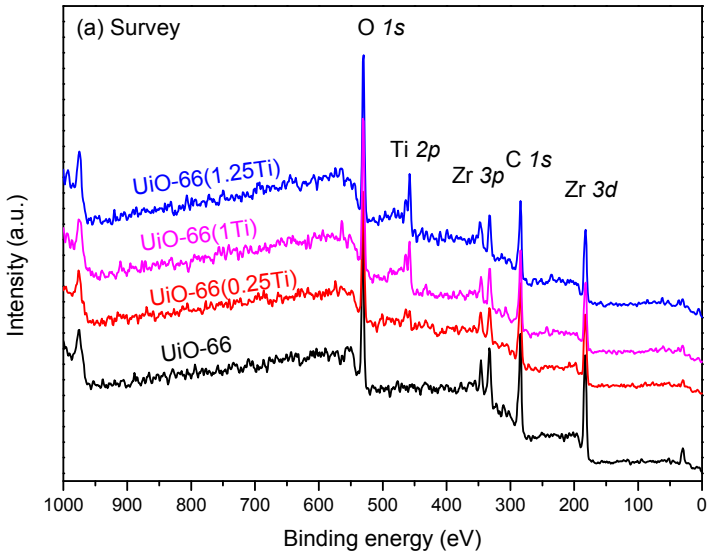

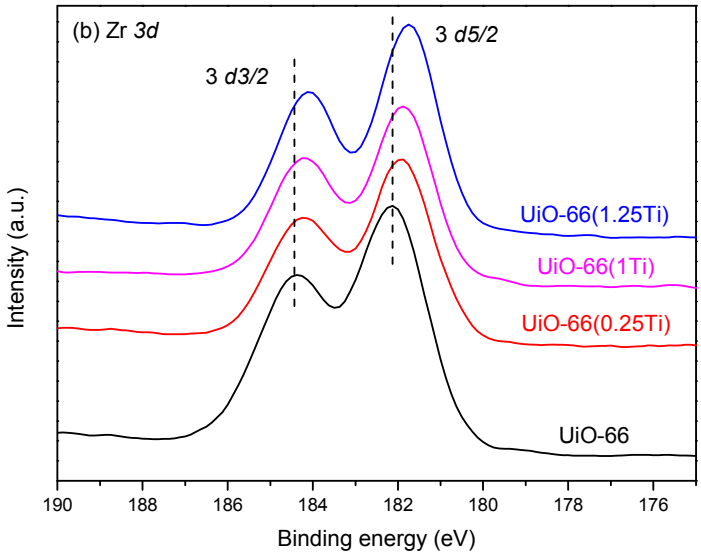

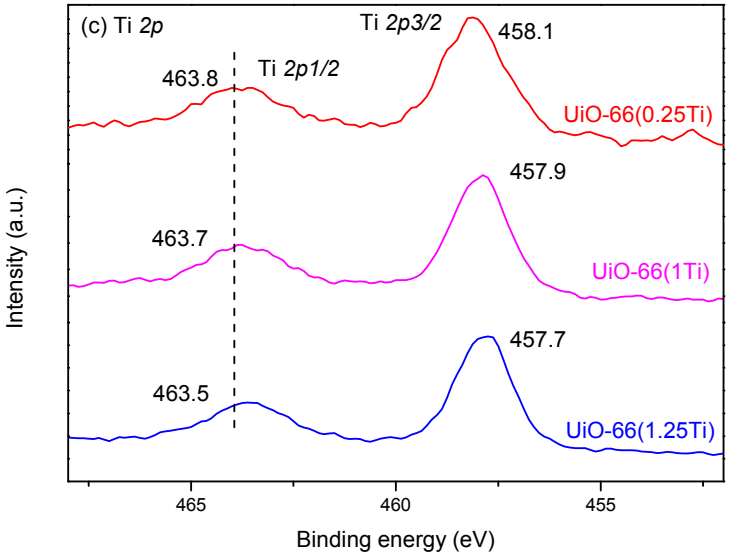

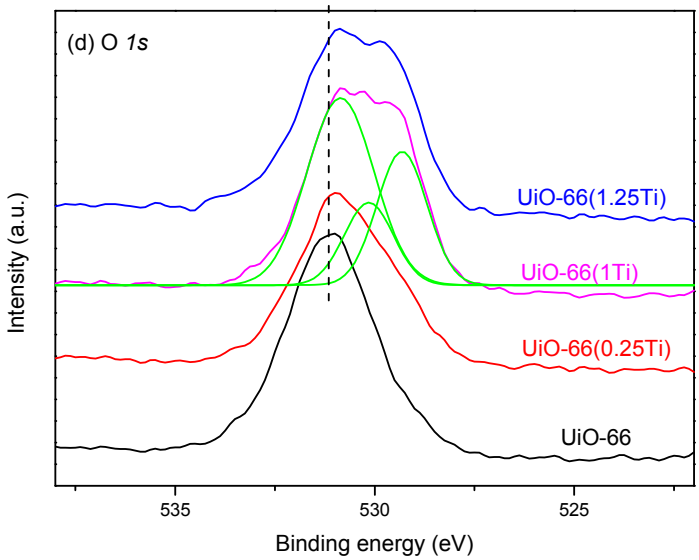

Figure 2. XPS spectra of (a) survey scan of UiO-66 and UiO-66(Ti) nanocomposites and the narrow scan in the (b) Zr *3d*, (c) Ti *2p*, and (d) O *1s* regions.

The textural morphology of UiO-66 and the selected UiO-66(1Ti) nanocomposite were investigated by SEM and TEM, and the observations are displayed in Figure 3. Obviously, the as-prepared UiO-66 presents spherical agglomerations instead of small crystals because of the smaller modulator concentrations compared with that reported in the literature.[51] UiO-66(1Ti) retained the similar morphology as UiO-66. Furthermore, no obvious differences of the morphologies could be observed from the TEM images. These observations suggest that Ti was truly incorporated into the UiO-66 framework to replace Zr as skeleton. This is in good agreement with the XRD (Figure 1) and XPS (Figure 2) results.

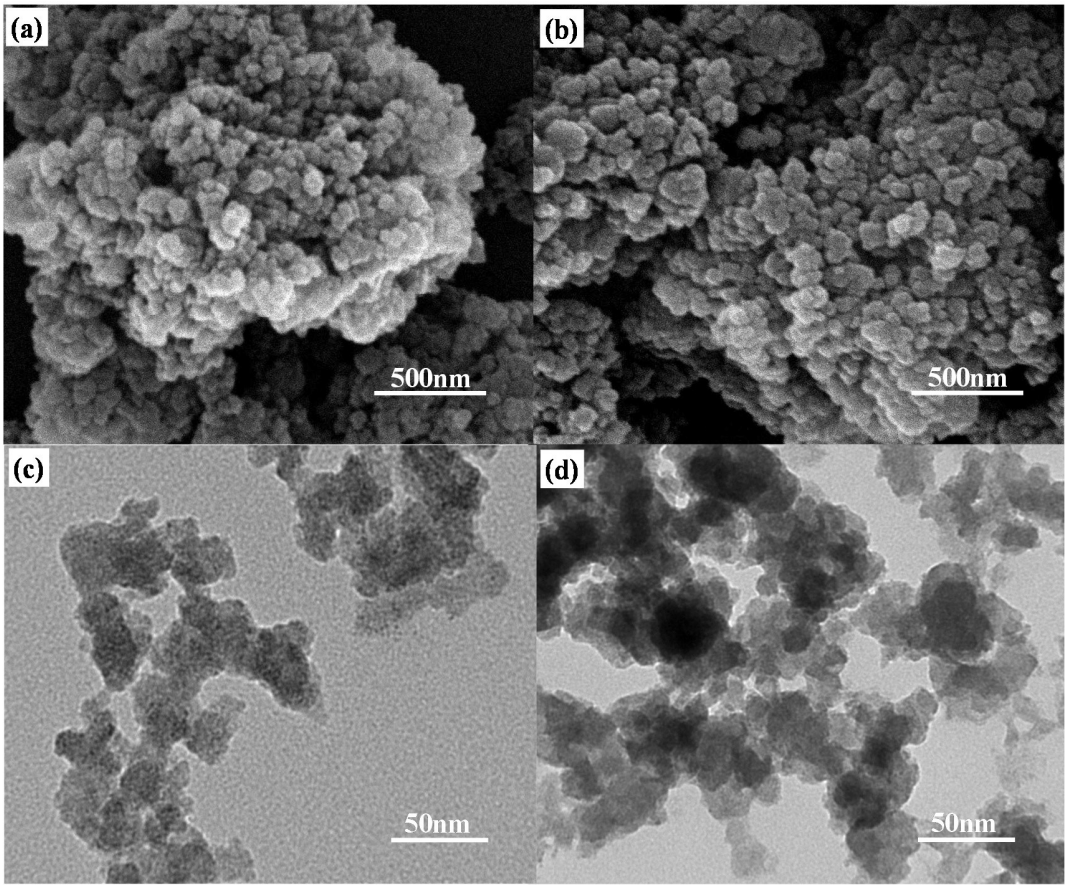

Figure 3. SEM images of (a) UiO-66, (b) UiO-66(1Ti), and TEM images of (c) UiO-66, (d) UiO-66(1Ti).

In addition, the porosity of UiO-66 and UiO-66(Ti) was also investigated by the BET analysis, and the results are displayed in Table 2. The specific surface area (S_{BET}) of UiO-66 is 889.6 m^2g^{-1}, and the S_{BET} of UiO-66(Ti) first decrease and then increase with an increasing Ti concentration, and UiO-66(1Ti) presents the lowest S_{BET} of 419.1 m^2g^{-1}. The decreased S_{BET} indicates that the pores in the UiO-(Ti) nanocomposites are smaller than the parent UiO-66. The lowest S_{BET} of UiO-66(1Ti) can be attributed to its poorest crystallinity. When Ti/Zr is larger than 1/1, the slightly increased S_{BET} could be attributed to the reformation of the uniform framework with Ti-O clusters as the skeleton.

Table 2. Specific surface areas of UiO-66 and UiO-66(Ti) nanocomposites.

Sample	S_{BET} (m^2 g^{-1})
UiO-66	889.6
UiO-66(0.25Ti)	710.4
UiO-66(0.5Ti)	626.3
UiO-66(0.75Ti)	608.3
UiO-66(1Ti)	419.1
UiO-66(1.25Ti)	451.2
UiO-66(1.5Ti)	590.4

The UV-visible absorption spectra are presented in Figure 4(a). UiO-66 shows two UV absorption peaks located at ca. 263 and 292 nm, which are ascribed to the UV adsorption of Zr-O oxo-clusters and the ligand-based adsorption influenced by the nearby metal centers, respectively. [43] However, these two peaks become broader and more intense after the titanium was incorporated into UiO-66. In addition, the UV-vis absorption edges of the as-prepared UiO-66(Ti) nanocomposites are shifted to longer wavelengths compared with that of UiO-66. The absorption bands seen in the near-visible and visible regions in UiO-66(Ti) are mainly attributed to the ligand-to-metal charge transfer.[52, 53] The red-shift of the UV-vis absorption edge implies the decrease in the band gap after the introduction of titanium species. The indirect band gap (E_g) values of UiO-66 and the UiO-66(Ti) are estimated by the Tauc equation ($\alpha h\nu = A(h\nu - E_g)^2$) (Figure 4(b)) using the UV-vis absorption data.[54-56] By extrapolating the linear portion of the $(\alpha h\nu)^{1/2}$ versus $h\nu$ curves to the X-axis, the indirect E_g values could be obtained. Results showed that the introduction of titanium species decreased the band gap of UiO-66. Thus, it is in favor of the ligand-to-metal charge transfer. This also supports that the titanium species behave as the electron donor in the UiO-66(Ti) nanocomposites. Based on these information, the energy level for the CB of the UiO-66(Ti) should be higher than that of the UiO-66, which is reported to be around ca. -0.09V (vs. NHE).[57] Furthermore, the light absorption of UiO-66(Ti) extends to the visible-light region with increasing Ti contents. Particularly, UiO-66(1.25Ti) shows the highest light absorption intensity in the

visible-light region, but the visible-light absorbance for UiO-66(1.5Ti) decreases significantly. The optical properties in the visible-light region strongly depended on the quantities of structural defects.[58, 59] According to the XRD patterns (Figure 1), UiO-66(1Ti) and UiO-66(1.25Ti) possess the lower crystallinity compared with other Ti/Zr molar ratios, thus lead to the formation of a larger amount of structural defects. This might be the reason that UiO-66(1Ti) and UiO-66(1.25Ti) own the better visible-light absorption properties. The crystallinity of UiO-66 was regenerated when the Ti/Zr was up to 1.5/1, suggesting that there were less amount of defects in UiO-66(1.5Ti). This might be the reason for the drop in its optical properties in the visible-light region.

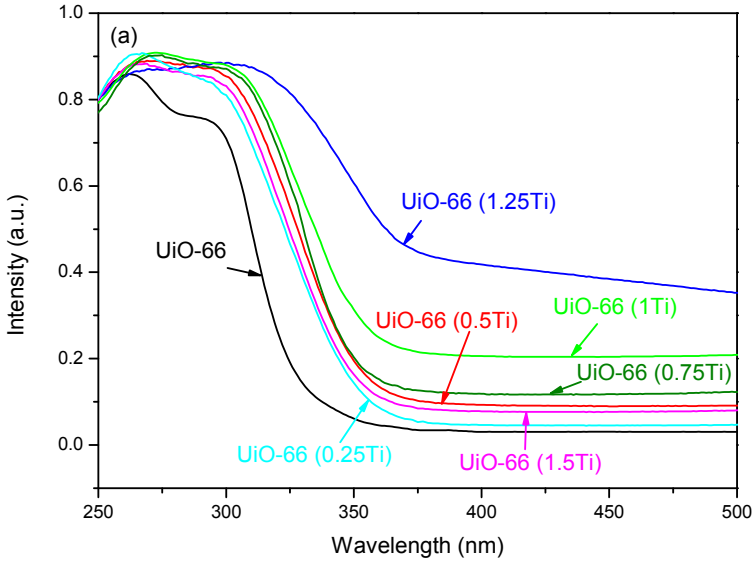

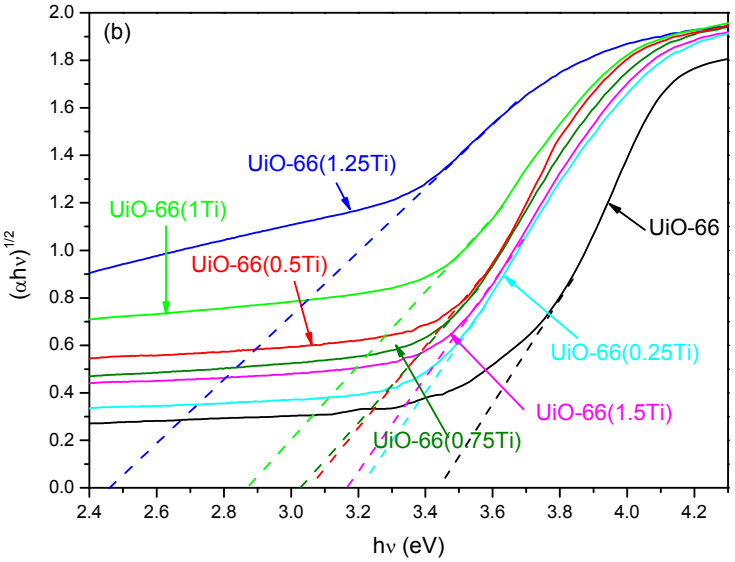

Figure 4. (a) UV-vis absorption spectra and (b) optical band gap determination by Tauc plot of UiO-66 and the UiO-66(Ti) nanocomposites with various Ti/Zr molar ratios.

The PL spectra of UiO-66 and the UiO-66(Ti) nanocomposites with various Ti/Zr molar ratios are shown in Figure 5. The PL intensities of UiO-66(Ti) nanocomposites decrease with increasing Ti contents except for UiO-66(1.5Ti). Moreover, the PL intensities became more intense after the introduction of titanium in the UiO-66 framework except for UiO-66(1Ti) and UiO-66(1.25Ti). The increased PL intensities can be ascribed to the high concentration of the photo-produced electron-hole pairs originated from the introduction of the titanium species. However, the weaker PL intensity of the UiO-66(1Ti) and UiO-66(1.25Ti) could be attributed to the structural defects stem from their lower crystallinity. The weaker PL intensity, the longer lifetime of the photo-generated electron-holes. The structural defects in the UiO-66(1Ti) and UiO-66(1.25Ti) can provide extra pathways for the migration of photo-generated electrons, thus facilitate the electron holes separation, and these lead to the longer lifetime of the photo-generated electron-holes. The enhanced optical properties are expected to improve the photocatalytic performance of UiO-66(Ti) toward a target

reaction.

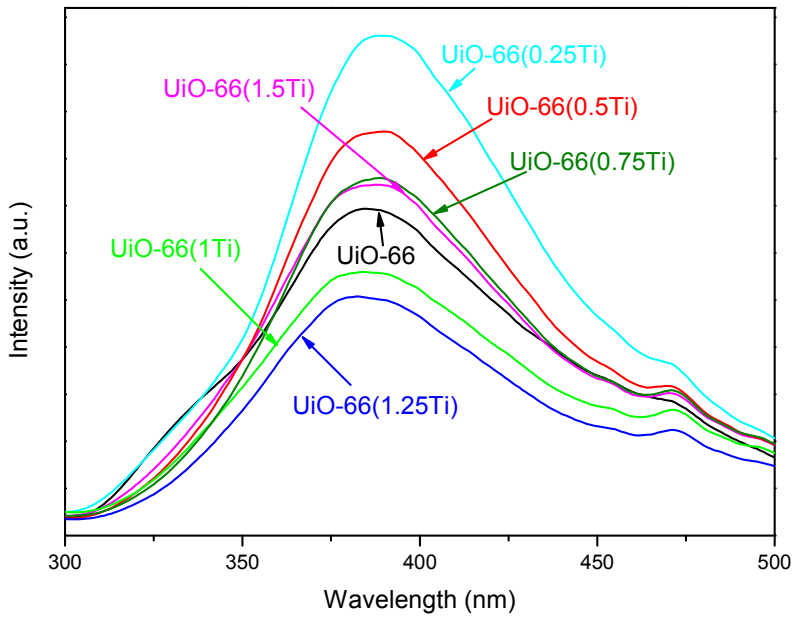

Figure 5. PL spectra of UiO-66 and the UiO-66(Ti) nanocomposites with various Ti/Zr molar ratios.

The removal of MB was selected as a model reaction to examine the adsorption and photocatalytic activities of the UiO-66(Ti) nanocomposites. The reaction system was first equilibrium for 80 min before it was transferred to the simulated sun light. The MB removal efficiency was estimated by the $100(1-C/C_0)\%$, where C_0 and C is the initial and actual MB concentration in the reaction system.[60] The result is shown in Figure 6. The MB adsorption over all the samples could achieve to equilibrium in 80 min. In detail, the MB removal efficiency in the first 30 min is very high, but it slightly decreased as the adsorption time goes, and there is no further adsorption after 60 min. UiO-66 presents the estimated MB removal efficiency of ca. 46.3% in 80 min without simulated sun light irradiation, and this is definitely due to its physical adsorption via a specific interaction, i.e., electrostatic interaction between the dyes and UiO-66.[13, 15] The MB removal efficiency over the UiO-66(Ti) first decreased and then increased with increasing Ti

contents. These are in consistent with the S_{BET} results (Table 2), and the UiO-66(1Ti) with the lowest S_{BET} possesses the poorest MB removal efficiency.

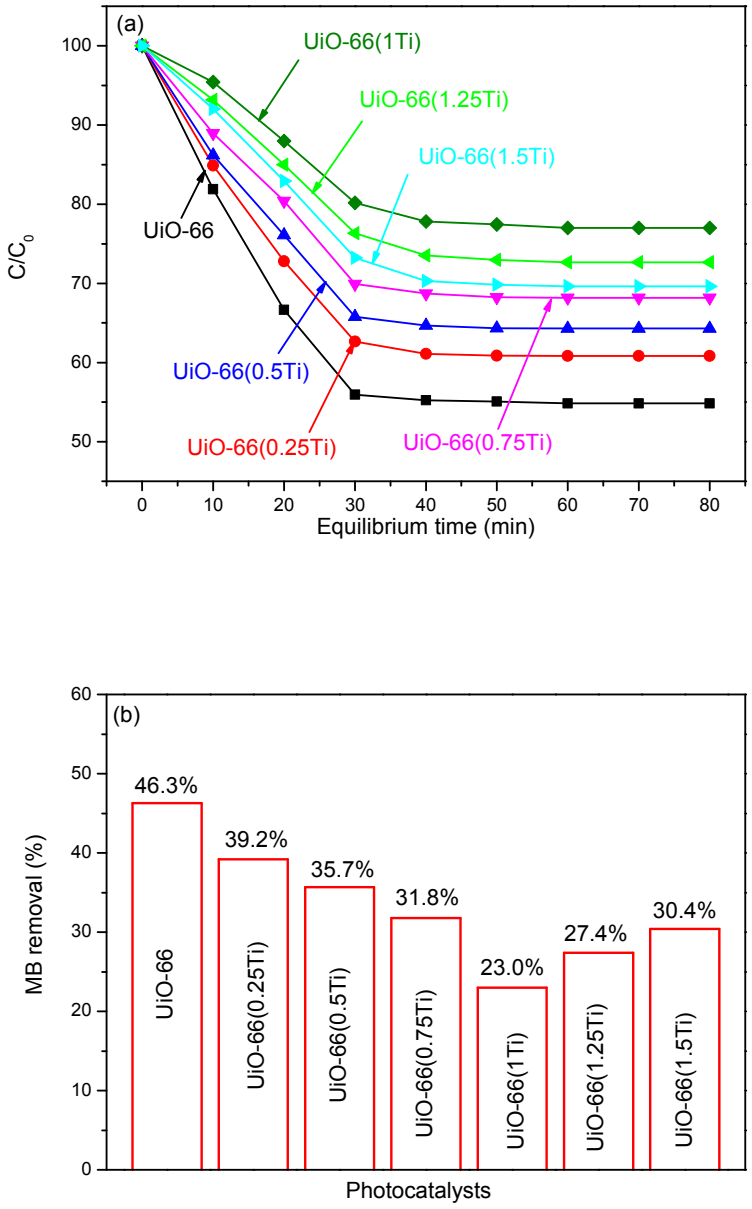

Figure 6. (a)Adsorption performance of UiO-66 and the UiO-66(Ti) nanocomposites with equilibrium time online and (b) MB removal efficiency of the samples after equilibrium for 80 min without simulated sun-light irradiation.

After the reaction system was equilibrium for 80 min, it was then exposed to the simulated sun-light. The photodegradation efficiency was estimated by 100(1- C/C_{80})%, where C_{80} is the MB concentration after equilibrium for 80 min in the reaction system. The photodegradation efficiencies over different samples are illustrated in Figure 7. The self-photosensitization of the organic dyes often happens under the light irradiation, and it matters little to the photocatalytic activity.[61, 62] It can be observed from Figure 7 that the UiO-66 barely shows any photocatalytic activity, therefore, the self-photosensitization of the methylene blue was not considered here. However, the incorporation with titanium could enhance its MB photodegradation efficiency greatly. The best MB degradation efficiency of 82.2% could be achieved over UiO-66(1.25Ti), which owns the strongest visible light absorption intensity (Figure 4) and the longest lifetime of the photo-generated electron-holes (Figure 5).

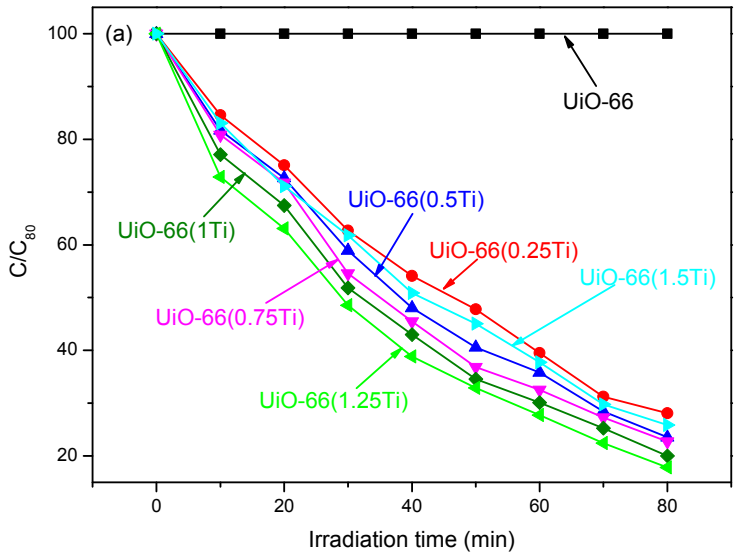

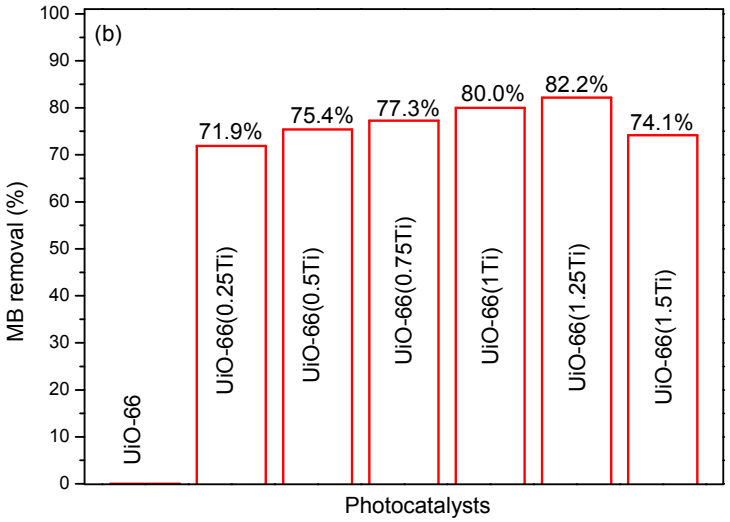

Figure 7. (a) Photocatalytic activity of UiO-66 and the UiO-66(Ti) nanocomposites with irradiation time online and (b) MB removal efficiency with simulated sun-light irradiation for 80 min.

The overall MB removal efficiency over the UiO-66 and UiO-66(Ti) were estimated by $100(1-C/C_0)\%$, and the results are shown in Figure 8. It is seen that the MB removal over the UiO-66(Ti) nanocomposites can be attributed to the effect of concurrent photo-degradation plus the absorption mechanism. Meanwhile, the photodegradation mechanism plays the major role in the MB removal. The best overall MB removal efficiency could be achieved to 87.1% over UiO-66(1.25Ti).

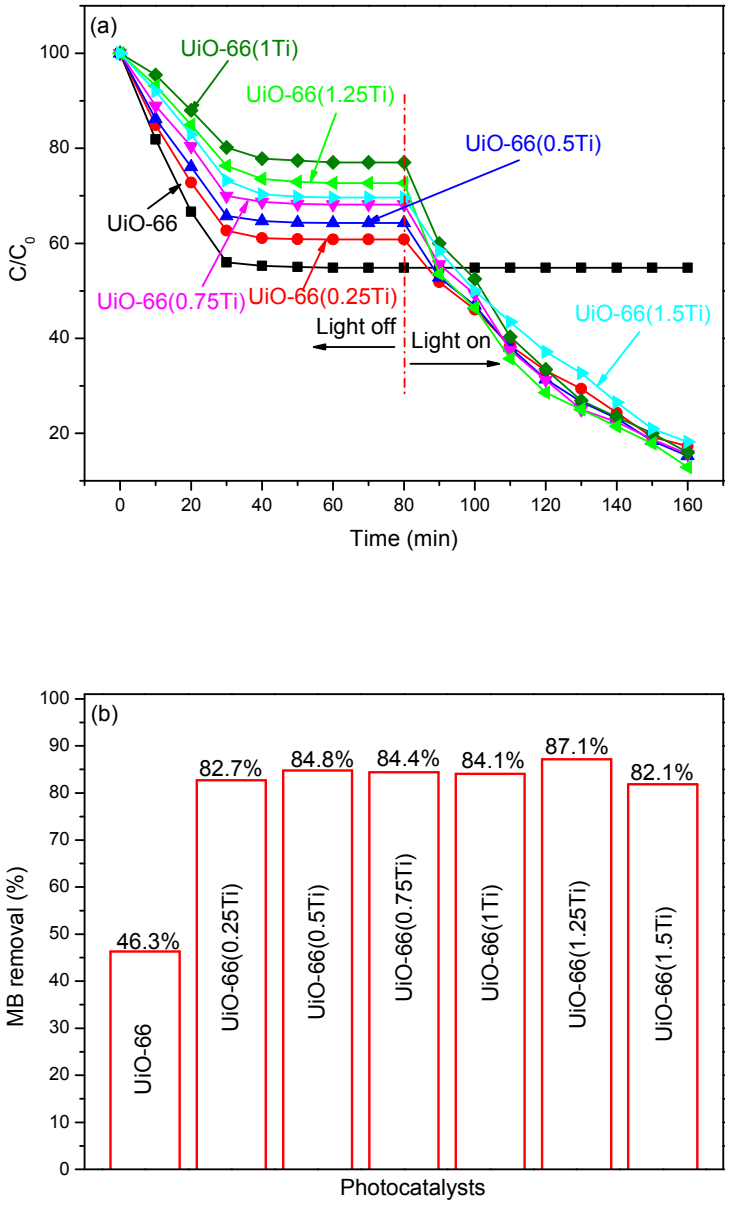

Figure 8. (a) Overall MB removal performance of the UiO-66 and UiO-66(Ti) nanocomposites with time online and (b) the overall MB removal efficiency with photocatalysts in the reaction system for 160 min. .

It has been widely investigated that the photodegradation of MB were strongly depended on the hydroxyl radicals (•OH) and superoxide ($\bullet O_2^-$) in the reaction system.[63]

In order to clarify the photocatalytic mechanism of UiO-66(Ti), trapping experiments of radicals and superoxide were used to detect the main active species in the photocatalytic process.[54, 61, 64] 1 mM isopropanol was added into the reaction system as the radical scavenger, and 1mM triethylamine was used to trap the superoxide. The catalytic results were presented in Figure 9(a). Apparently, the MB photodegradation efficiency with the isopropanol or triethylamine was inferior to the reaction system without the radical scavenger. This suggests that the radicals and superoxide were the main active species in this photocatalytic system. The possible organic dye degradation mechanism over the UiO-66(Ti) could be proposed as follow equations, and the detailed mechanism is summarized in Figure 9(b).

$$\text{UiO-66(Ti)} + h\nu \longrightarrow e^- + h^+ \quad (1)$$

$$e^- + O_2 \longrightarrow \cdot O_2^- \quad (2)$$

$$h^+ + OH^- \longrightarrow \cdot OH \quad (3)$$

As it is observed from the UV-vis absorption of the UiO-66 and UiO-66(Ti) presented in Figure 4, the addition of Ti in the UiO-66 could enhance its optical properties by narrowing its band gap to less than 3.2 eV. The illumination of UiO-66(Ti) by simulated sun-light irradiation with energy equal to or greater than its band gap can excites electrons (e^-) from the HOMO energy level to the LUMO energy level and produces holes (h^+) in the valence band. The photo-generated electrons (e^-) in LUMO can be trapped by the dissolved molecular oxygen in the reaction system to form superoxide ($\bullet O_2^-$), which will react with H^+ in the water to form hydroxyl radicals ($\bullet$OH). Meanwhile, the photo-induced positive holes (h^+) in the HOMO bands can directly interact with the active OH groups in surface adsorbed water (H_2O) to produce the hydroxyl radicals ($\bullet$OH). The formed hydroxyl radicals ($\bullet$OH) possess strong oxidation ability. In the next step, the organic pollutants can be concurrently degraded to CO_2, H_2O and other intermediates during the photolysis process by interacting with the hydroxyl radicals ($\bullet$OH) or superoxide ($\bullet O_2^-$).

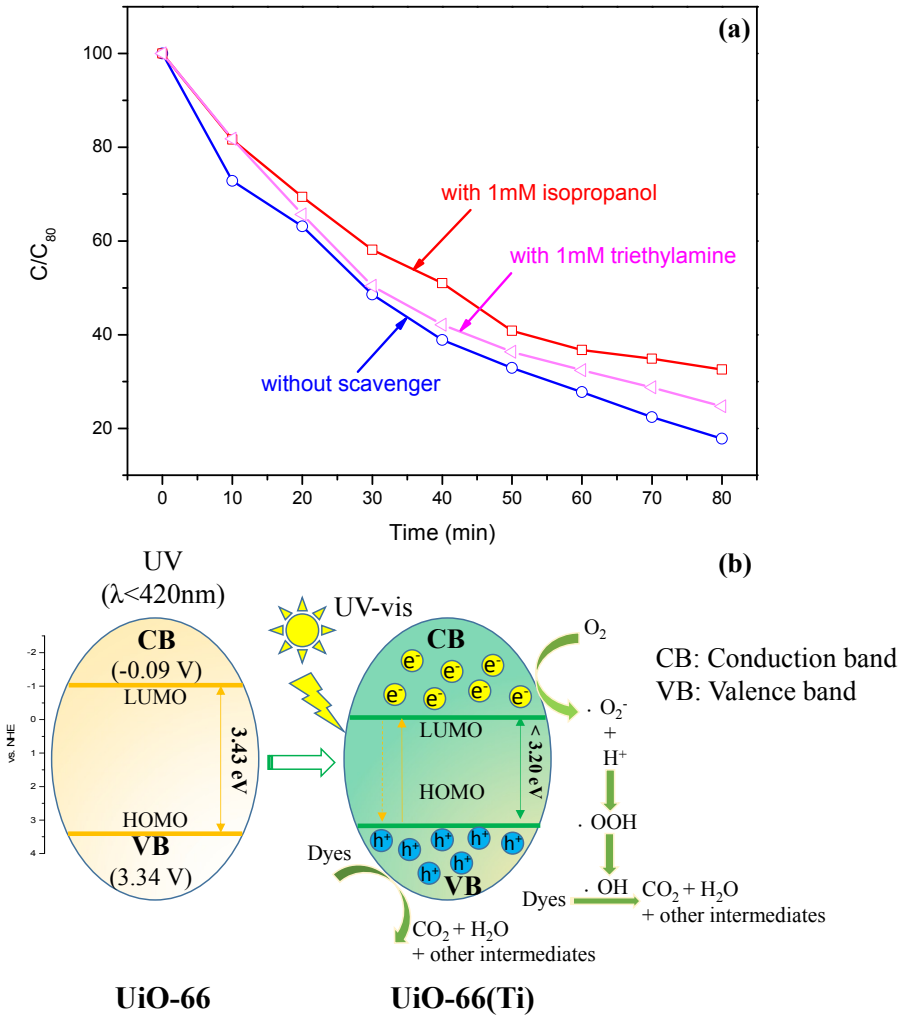

Figure 9. (a) Photodegradation efficiency of MB over UiO-66(1.25Ti) in the reaction system with and without scavengers under UV-vis light irradiation, (b) scheme of the proposed photocatalysis mechanism.

Based on the XPS, XRD, SEM and TEM characterizations of the UiO-66 and UiO-66(Ti), the addition of Ti can narrow the band gap of UiO-66, and this is majorly attributed to the electron donor properties of Ti. These result in the enhanced light absorption properties of the UiO-66(Ti) (Figure 4). A higher UV-vis light absorption intensity of a photocatalyst is expected to supply more photo-generated electrons and holes, which will be benefit for the photocatalytic activity. These are the reasons why the

photocatalytic activities of UiO-66(Ti) presented in Figure 7 follow the order of the UV-vis adsorption intensities shown in Figure 4. On the other hand, the crystallinity of the UiO-66 is decreased after the incorporation with Ti because of the mismatch atom size of the Zr and Ti. The non-uniform porous properties can lead to numerous structural defects of the UiO-66(Ti), which can provide extra migration pathways for the photo-generated electron-holes. This will prolong the lifetime of the photo-generated electron-holes (Figure 5), leading to an enhancement of the photocatalytic performance (Figure 7). Meanwhile, non-uniform porous structures will sacrifice the S_{BET}. The higher S_{BET} is beneficial for the MB adsorption (Figure 6). From the overall MB remove efficiency presented in Figure 8, the MB removal over UiO-66(Ti) nanocomposites could be attributed to the results of adsorption as well as the photodegradation mechanisms.

4. Conclusion

In summary, a new type titanium fabricated MOF was synthesized using UiO-66 as the substrate (UiO-66(Ti)) via a facial approach. The titanium behaved as the electron donor via the formation of oxo-bridged hetero-Zr-Ti clusters, and thus leads to enhanced optical properties compared to the parent UiO-66. However, the UiO-66(Ti) nanocomposites exhibited lower surface area. The removal of MB over the UiO-66(Ti) nanocomposites could be attributed to the synergetic effects of light absorption intensity, efficient separation of the photo-generated electron-hole pairs as well as their porous properties. The highest MB removal efficiency of ca. 87.1% over UiO-66(1.25Ti) could be achieved. This work provides a new approach to remove organic pollutants via the cooperation of adsorption and photo-degradation mechanisms by exploring new types of

photocatalysts with large specific surface areas.

Acknowledgement

Y. Z. thanks the support by the startup foundation for introducing talent of Nanjing University of Information Science & Technology (NUIST) (2241131301102).

References

1. L. Shen, M. Luo, Y. Liu, R. Liang, F. Jing and L. Wu, *Appl. Catal. B.*, 2015, **166–167**, 445-453.
2. J. Lee, O. K. Farha, J. Roberts, K. A. Scheidt, S. T. Nguyen and J. T. Hupp, *Chem. Soc. Rev.*, 2009, **38**, 1450-1459.
3. L. Ma, C. Abney and W. Lin, *Chem. Soc. Rev.*, 2009, **38**, 1248-1256.
4. Z. Guo, H. Wu, G. Srinivas, Y. Zhou, S. Xiang, Z. Chen, Y. Yang, W. Zhou, M. O'Keeffe and B. Chen, *Angew. Chem. Int. Edit.*, 2011, **50**, 3178-3181.
5. T. L. Hu, H. Wang, B. Li, R. Krishna, H. Wu, W. Zhou, Y. Zhao, Y. Han, X. Wang, W. Zhu, Z. Yao, S. Xiang and B. Chen, *Nat. Commun.*, 2015, **6**, 10.1038/ncomms8328.
6. Y. Li and R. T. Yang, *Langmuir*, 2007, **23**, 12937-12944.
7. A. Car, C. Stropnik and K. V. Peinemann, *Desalination*, 2006, **200**, 424-426.
8. P. Li, Y. He, Y. Zhao, L. Weng, H. Wang, R. Krishna, H. Wu, W. Zhou, M. O'Keeffe and Y. Han, *Angew. Chem.*, 2015, **127**, 584-587.
9. J. R. Li, R. J. Kuppler and H. C. Zhou, *Chem. Soc. Rev.*, 2009, **38**, 1477-1504.
10. H. M. Wen, B. Li, H. Wang, C. Wu, K. Alfooty, R. Krishna and B. Chen, *Chem. Commun.*, 2015, **51**, 5610-5613.
11. P. Horcajada, T. Chalati, C. Serre, B. Gillet, C. Sebrie, T. Baati, J. F. Eubank, D. Heurtaux, P. Clayette and C. Kreuz, *Nat. Mater.*, 2010, **9**, 172-178.
12. P. Horcajada, C. Serre, G. Maurin, N. A. Ramsahye, F. Balas, M. Vallet-Regi, M. Sebban, F. Taulelle and G. Férey, *J. Am. Chem. Soc.*, 2008, **130**, 6774-6780.
13. E. Haque, J. W. Jun and S. H. Jhung, *J. Hazard. Mater.,* 2011, **185**, 507-511.
14. A. Banerjee, R. Gokhale, S. Bhatnagar, J. Jog, M. Bhardwaj, B. Lefez, B.

Hannoyer and S. Ogale, *J. Mater. Chem.*, 2012, **22**, 19694-19699.
15. E. Haque, J. E. Lee, I. T. Jang, Y. K. Hwang, J.-S. Chang, J. Jegal and S. H. Jhung, *J. Hazard. Mater.,* 2010, **181**, 535-542.
16. M. C. Das, H. Xu, Z. Wang, G. Srinivas, W. Zhou, Y. F. Yue, V. N. Nesterov, G. Qian and B. Chen, *Chem. Commun.,* 2011, **47**, 11715-11717.
17. Z. Guo, H. Xu, S. Su, J. Cai, S. Dang, S. Xiang, G. Qian, H. Zhang, M. O'Keeffe and B. Chen, *Chem. Commun.,* 2011, **47**, 5551-5553.
18. Y. Xiao, Y. Cui, Q. Zheng, S. Xiang, G. Qian and B. Chen, *Chem. Commun.,* 2010, **46**, 5503-5505.
19. A. Di Paola, E. García-López, G. Marcì and L. Palmisano, *J. Hazard. Mater.,* 2012, **211–212**, 3-29.
20. H. Khajavi, J. Gascon, J. M. Schins, L. D. A. Siebbeles and F. Kapteijn, *J. Phys. Chem. C.*, 2011, **115**, 12487-12493.
21. M. Nasalevich, M. Van der Veen, F. Kapteijn and J. Gascon, *CrystEngComm*, 2014, **16**, 4919-4926.
22. L. Shen, W. Wu, R. Liang, R. Lin and L. Wu, *Nanoscale*, 2013, **5**, 9374-9382.
23. M. Alvaro, E. Carbonell, B. Ferrer, F. X. Llabrés i Xamena and H. Garcia, *Chem. Eur. J.*, 2007, **13**, 5106-5112.
24. C. G. Silva, A. Corma and H. García, *J. Mater. Chem.,* 2010, **20**, 3141-3156.
25. J. He, Z. Yan, J. Wang, J. Xie, L. Jiang, Y. Shi, F. Yuan, F. Yu and Y. Sun, *Chem. Commun.,*2013, **49**, 6761-6763.
26. H. Y. Sun, C. B. Liu, Y. Cong, M. H. Yu, H. Y. Bai and G.-B. Che, *Inorg. Chem. Commun.*. 2013, **35**, 130-134.
27. H. Chen and J. Zhao, *Adsorption*, 2009, **15**, 381-389.
28. S. T. Ong, P. S. Keng, W. N. Lee, S. T. Ha and Y. T. Hung, *Water*, 2011, **3**, 157-176.
29. S. H. Huo and X. P. Yan, *J. Mater. Chem.*, 2012, **22**, 7449-7455.
30. G. Crini, *Bioresource. Technol.*, 2006, **97**, 1061-1085.
31. I. K. Konstantinou and T. A. Albanis, *Appl. Catal. B.*, 2004, **49**, 1-14.
32. A. K. Verma, R. R. Dash and P. Bhunia, *J. Environ. Manage.*, 2012, **93**, 154-168.
33. L. S. Andrade, L. A. M. Ruotolo, R. C. Rocha-Filho, N. Bocchi, S. R. Biaggio, J. Iniesta, V. García-Garcia and V. Montiel, *Chemosphere*, 2007, **66**, 2035-2043.
34. C. Pearce, J. Lloyd and J. Guthrie, *Dyes. Pigments*, 2003, **58**, 179-196.
35. V. K. Gupta, A. Mittal, R. Jain, M. Mathur and S. Sikarwar, *J. Colloid. Interf. Sci.*, 2006, **303**, 80-86.
36. S. K. Alpat, Ö. Özbayrak, Ş. Alpat and H. Akçay, *J. Hazard. Mater.*, 2008, **151**, 213-220.
37. X. Lü, W. Yang, Z. Quan, T. Lin, L. Bai, L. Wang, F. Huang and Y. Zhao, *J. Am. Chem. Soc.*, 2014, **136**, 419-426.
38. B. Ohtani, *J. Photoch. Photobio. C.*, 2010, **11**, 157-178.
39. T. L. Thompson and J. T. Yates Jr, *Chem. Rev.*, 2006, **106**, 4428-4453.

40. E. S. Aazam, *J. Ind. Eng. Chem.*,2014, **20**, 4033-4038.
41. Q. Chen, Q. He, M. Lv, Y. Xu, H. Yang, X. Liu and F. Wei, *Appl. Surf. Sci.*, 2015, **327**, 77-85.
42. E. Haque, V. Lo, A. I. Minett, A. T. Harris and T. L. Church, *J. Mater. Chem. A.*, 2014, **2**, 193-203.
43. D. Sun, W. Liu, M. Qiu, Y. Zhang and Z. Li, *Chem. Commun.,* 2015, **51**, 2056-2059.
44. J. W. Park, Y. J. Park and C. H. Jun, *Chem Commun*, 2011, **47**, 4860-4871.
45. M. Kandiah, M. H. Nilsen, S. Usseglio, S. Jakobsen, U. Olsbye, M. Tilset, C. Larabi, E. A. Quadrelli, F. Bonino and K. P. Lillerud, *Chem. Mater.*, 2010, **22**, 6632-6640.
46. J. H. Cavka, S. Jakobsen, U. Olsbye, N. Guillou, C. Lamberti, S. Bordiga and K. P. Lillerud, *J. Am. Chem. Soc.*,2008, **130**, 13850-13851.
47. M. Hino and K. Arata, *Chem. Commun.,* 1988, 1259-1260.
48. M. B. Gawande, P. S. Branco, K. Parghi, J. J. Shrikhande, R. K. Pandey, C. Ghumman, N. Bundaleski, O. Teodoro and R. V. Jayaram, *Catal. Sci. Technol.*, 2011, **1**, 1653-1664.
49. C. He, Y. Yu, X. Hu and A. Larbot, *Appl. Surf. Sci.*, 2002, **200**, 239-247.
50. Y. L. Lin, T. J. Wang and Y. Jin, *Powder. Technol*, 2002, **123**, 194-198.
51. G. Wißmann, A. Schaate, S. Lilienthal, I. Bremer, A. M. Schneider and P. Behrens, *Micropor. Mesopor. Mat.*, 2012, **152**, 64-70.
52. S. Bordiga, C. Lamberti, G. Ricchiardi, L. Regli, F. Bonino, A. Damin, K.-P. Lillerud, M. Bjorgen and A. Zecchina, *Chem. Commun.*, 2004, 2300-2301.
53. W. Lin and H. Frei, *J. Am. Chem. Soc.*, 2005, **127**, 1610-1611.
54. Alamgir, W. Khan, S. Ahmad, M. Mehedi Hassan and A. H. Naqvi, *Opt. Mater*, 2014, **38**, 278-285.
55. J. Tauc, R. Grigorovici and A. Vancu, *Phys. Status. Solidi. B.*, 1966, **15**, 627-637.
56. N. Bayal and P. Jeevanandam, *Ceram. Int.*, 2014, **40**, 15463-15477.
57. R. Lin, L. Shen, Z. Ren, W. Wu, Y. Tan, H. Fu, J. Zhang and L. Wu, *Chemical Communications*, 2014, **50**, 8533-8535.
58. Y. Iwayam *Chem. Commun.,*a, J. Yamanaka, Y. Takiguchi, M. Takasaka, K. Ito, T. Shinohara, T. Sawada and M. Yonese, *Langmuir*, 2003, **19**, 977-980.
59. F. Zuo, L. Wang, T. Wu, Z. Zhang, D. Borchardt and P. Feng, *J. Am. Chem. Soc.*, 2010, **132**, 11856-11857.
60. Z. R. Tang, Q. Yu and Y. J. Xu, *RSC. Adv*, 2014, **4**, 58448-58452.
61. L. Yuan, M. Q. Yang and Y. J. Xu, *Nanoscale*, 2014, **6**, 6335-6345.
62. Z. Chen, N. Zhang and Y. J. Xu, *CrystEngComm*, 2013, **15**, 3022-3030.
63. D. Das, N. Biswal, S. Martha and K. Parida, *J. Mol. Catal. A: Chem.*, 2011, **349**, 36-41.
64. M. Muneer, R. Philip and S. Das, *Res. Chem. Intermed.*, 1997, **23**, 233-246.

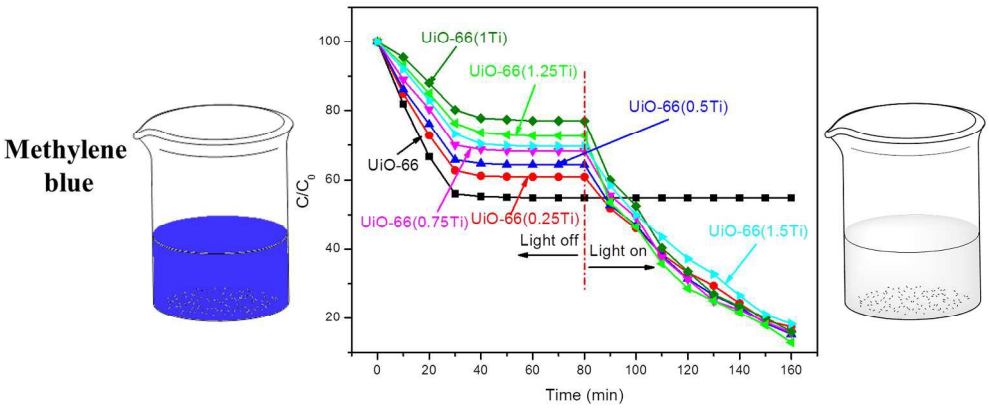

Dual function of the adsorption and photodegradation for the Methylene blue removal over the UiO-66(Ti) nanocomposites.

846x465mm (150 x 150 DPI)